Equilibrium Shapes of Planar Elastic Membranes

Gary R. Marple[1], Prashant K. Purohit[2], and Shravan Veerapaneni[1]
[1]*Department of Mathematics, University of Michigan,*
Ann Arbor, MI 48109, USA
[2]*Department of Mechanical Engineering and Applied Mechanics,*
University of Pennsylvania,
Philadelphia, PA 19104, USA

(Dated: June 9, 2015)

Using a rod theory formulation, we derive equations of state for a thin elastic membrane subjected to several different boundary conditions – clamped, simply supported and periodic. The former is applicable to membranes supported on a softer substrate and subjected to uniaxial compression. We show that a wider family of quasi-static equilibrium shapes exist beyond the previously obtained analytical solutions. In the latter case of periodic membranes, we were able to derive exact solutions in terms of elliptic functions. These equilibria are verified by considering a fluid-structure interaction problem of a periodic, length-preserving bilipid membrane modeled by the Helfrich energy immersed in a viscous fluid. Starting from an arbitrary shape, the membrane dynamics to equilibrium are simulated using a boundary integral method.

PACS numbers: 68.08.-p, 47.63.-b, 47.55.-t

INTRODUCTION

Understanding the wrinkling and folding patterns of elastic sheets over a soft substrate has received much attention recently owing to a large number of practical applications [1]. Recent experiments of [2] appeared to show that a wrinkle to fold transition of the sheet occurs whenever it is compressed beyond a certain threshold. The fold patterns are highly localized which have also been reproduced numerically in [2]. Elegant analytic solutions for the fold shapes have been derived in [3] (and extended recently to sheets of finite length in [4]) by showing that the Euler's elastica equation governing the elastic sheet belongs to the stationary-sine-Gordon-modified-KdV hierarchy, which is integrable. Two classes of solutions, corresponding to a symmetric and an anti-symmetric fold, have been reported. However, these solutions are restricted to the primary single-fold shapes. More recently [5, 6] have also used a rod theory formulation to study the shapes of floating elasticas. In [6], the authors first linearize the rod equations and get buckling thresholds as well as symmetric and antisymmetric mode shapes. Then they perform a non-linear post-buckling analysis to get the shapes of the elastica with large deflections of the rod. Finally, they check for the stability of these post-buckled shapes. [6] resolve the forces in the rod in a lab-fixed coordinate system and solve the resulting non-linear ODEs numerically to get the post-buckled shapes.

In this paper, we present new analytical solutions for the equilibrium shapes. Furthermore, we obtain more general multiple-fold shapes numerically by solving a set of first-order ordinary differential equations (ODEs) derived using large deflection theory of rods. Unlike the far-field boundary conditions applied in [3] (for the sake of deriving exact solutions), we apply clamped boundary conditions. This is consistent with the experimental set-up of [2] wherein the lateral edges of a thin polymer sheet resting on the surface of water are clamped while the sheet itself is compressed laterally. By simply varying the applied strain, which enters as a boundary condition in our formulation, we get shapes with varying complexity from smooth to highly localized to nearly touching configurations. In contrast to [6], we resolve the force in the rod along coordinates that are tangential and normal to the rod and obtain analytical solutions to the resulting non-linear ODEs.

Using the same formalism, we consider another important problem, that of determining the periodic equilibrium shapes of lipid membranes immersed in a viscous fluid. Periodic equilibria of lipid bilayers in the form of minimal surfaces (with cubic symmetry) have been known for a long time [7]. Periodic cylindrical equilibria are also known [8]. Indeed, such periodic shapes are observed in cellular organelles such as mitochondria, chloroplasts, and endoplasmic reticula [9, 10]. Periodic shapes with cylindrical symmetry have been realized in suspended lipid bilayers [11]. Moreover, periodic membrane mechanics is often used as a paradigm for understanding the complex multi-physics of soft particles such as vesicles and red blood cells. For example, [12] studied the interplay of membrane compositional dynamics with solvent hydrodynamics while [13] considered the vesicle electrohydrodynamics.

Building on our previous work on closed vesicles [14], we derive exact solutions in terms of elliptic functions to the ODEs of rod theory formulation with periodic boundary conditions. Excess length characterizes the obtained equilibrium shapes. We show that single-fold shapes have lower elastic energy compared to multiple-fold shapes for a fixed excess length. While useful in their own right, the exact solutions, perhaps more importantly, can be used for validating numerical schemes that are applicable in the broader context of simulating biomembranes in viscous fluids. We formulate and implement a boundary integral method to simulate the dynamics of a periodic lipid bilayer membrane suspended in a viscous fluid. The membrane dynamics are characterized by a competition between elastic energy, local inextensibility, and non-local hydrodynamic forces. We develop a high-order method to solve the integro-differential equations for membrane evolution to equilibrium by the use of Fourier representations and a high-order singular integration scheme. We show that for any arbitrary initial profile, the membrane always relaxes to one of the exact solutions we derived using the rod theory formulation.

ROD-THEORY FORMULATION

In this section, we provide a rod-theory based approach for computing equilibrium configurations of planar membranes. Since we focus primarily on cylindrical membrane shapes, it is sufficient to think of the membrane as an inextensible planar rod [15]. Indeed, recent experiments on membranes or thin films at the interface between two liquids have demonstrated a variety of shapes that are similar to those obtained in our computations. All of these membrane shapes are cylindrical so that curvature is a scalar variable, just as it is for a planar rod. At any cross-section of this rod located at arc length s, there are two components of the internal force $F_x(s)$ and $F_y(s)$ and one internal moment $M(s)$. The tangent to the rod makes an angle $\theta(s)$ with the laboratory x-axis. Therefore,

$$\cos\theta = \frac{dx}{ds} \quad \text{and} \quad \sin\theta = \frac{dy}{ds}. \tag{1}$$

The equilibrium equations for the rod are well-known and are given by [16]

$$\begin{aligned} \frac{dF_x}{ds} + b_x &= 0, & (2)\\ \frac{dF_y}{ds} + b_y &= 0, & (3)\\ \frac{dM}{ds} - F_x\sin\theta + F_y\cos\theta + m &= 0, & (4) \end{aligned}$$

where $b_x(s)$ and $b_y(s)$ are body forces per unit length and $m(s)$ is a body moment per unit length. In experiments on thin films at liquid interfaces, the body forces arise from hydrostatic pressure exerted by a liquid column on the film. Such a pressure acts normal to the surface $\mathbf{n}$ of the film and takes the form $\mathbf{b}(s) = b(s)\mathbf{n}$, where $b(s)$ is a scalar function. Since there are no body moments in the films studied in these experiments, we will set $m = 0$ everywhere. Given this form of the body force, it is natural to resolve the internal force $\mathbf{F}$ in the rod along the tangent $\mathbf{t}$ and normal $\mathbf{n}$. Then, $\mathbf{F} = F_t\mathbf{t} + F_n\mathbf{n}$ and the equilibrium equations can be written as

$$\begin{aligned} \frac{dF_t}{ds} + F_n\kappa &= 0, & (5)\\ \frac{dF_n}{ds} - F_t\kappa + b &= 0, & (6)\\ \frac{dM}{ds} + F_n &= 0, & (7) \end{aligned}$$

where $\kappa = \frac{d\theta}{ds}$ is the curvature and the rod is assumed to be inextensible. The tangent and normal to the rod are related through the standard Frenet-Serret formulas on the plane, given by

$$\frac{d\mathbf{t}}{ds} = -\kappa\mathbf{n} \quad \text{and} \quad \frac{d\mathbf{n}}{ds} = \kappa\mathbf{t}. \tag{8}$$

We also assume that the moment M and curvature κ are related through $M = K_b\kappa$ where K_b is a bending modulus of the membrane. Then, (5) and (7) can be combined to yield

$$F_t = \frac{K_b}{2}\kappa^2 + C, \tag{9}$$

where C is a constant that must be determined from the boundary conditions. When we plug (9) into (6), we get

$$K_b\frac{d^2\kappa}{ds^2} + \frac{K_b}{2}\kappa^3 + C\kappa - b = 0. \tag{10}$$

If we recognize $-C/K_b$ as the tension σ and $-b/K_b$ as the pressure difference p between the bottom and top of the film, then this is the same equation that was solved previously for closed vesicles [14], assuming a constant pressure difference.

ANALYTICAL SOLUTIONS

In this section, we derive analytic solutions to (10) for three kinds of boundary conditions—clamped, periodic and simply supported—in terms of the Jacobi elliptic functions which are defined using the integral $u = \int_0^\phi 1/\sqrt{1 - m\sin^2\theta}\, d\theta$ as

$$\begin{aligned} \mathrm{sn}(u|m) &= \sin(\phi), & (11)\\ \mathrm{cn}(u|m) &= \cos(\phi), & (12)\\ \mathrm{dn}(u|m) &= \sqrt{1 - m\sin^2\phi}. & (13) \end{aligned}$$

Clamped boundary conditions

For clamped boundary conditions, we solve (10) with a non-zero pressure difference between the two sides of

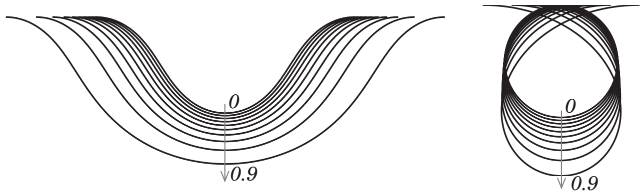

FIG. 1: *Plot of equilibrium shapes corresponding to the exact solutions* (14) *and* (19) *for different values of* $m^2 = \{0, 0.1, 0.2, \ldots, 0.9\}$.

the film. In order to illustrate this method and to relate to the experimental results of [2], we assume that $b = -ky = -\rho g y$, where ρ is the density difference between the liquids on the two sides of the film, g is the acceleration due to gravity, and $k = \rho g$ is the stiffness of the "substrate". Under this assumption, an analytical solution to (10) is given by

$$\kappa(s) = \frac{2\sqrt{1-m^2}}{\mathrm{dn}(s|m)}, \tag{14}$$

for which

$$\frac{C}{K_b} = m^2 - 2 - \frac{\rho g}{K_b m^2}. \tag{15}$$

This gives

$$\begin{aligned} \theta(s) &= 2\sqrt{1-m^2}\frac{\mathrm{sn}(s|m)\mathrm{cn}(s|m)}{\mathrm{dn}^2(s|m)}, && (16) \\ x(s) &= \int \left(2\frac{\mathrm{cn}^2(s|m)}{\mathrm{dn}^2(s|m)} - 1\right) ds, && (17) \\ y(s) &= 2\frac{\sqrt{1-m^2}}{m^2}\frac{1}{\mathrm{dn}(s|m)}. && (18) \end{aligned}$$

Clearly, $\theta(s = \pm K(m)) = 0$ where $K(m)$ is the complete elliptic integral of the first kind. If we take $L = 2K(m)$ then this solution represents clamped-clamped boundary conditions. The parameter m can be determined by enforcing $x(\frac{L}{2}) - x(-\frac{L}{2}) = \frac{L}{1+\epsilon_{pre}}$ where ϵ_{pre} is a prescribed pre-strain. Alternatively, ϵ_{pre} is determined by the compression applied on the film which specifies the end-to-end distance $x(\frac{L}{2}) - x(-\frac{L}{2})$. We can always re-scale the length L by a length scale λ such that $\frac{L}{\lambda} = K(m)$. The constant C must then be modified accordingly. Another solution to (10) is

$$\kappa(s) = 2\mathrm{dn}(s|m), \tag{19}$$

for which

$$\frac{C}{K_b} = m^2 - 2 + \frac{\rho g}{K_b m^2}. \tag{20}$$

This gives

$$\begin{aligned} \theta(s) &= 2\sin^{-1}(\mathrm{sn}(s|m)), && (21) \\ x(s) &= \frac{2}{m^2}E(s|m) + (1 - \frac{2}{m^2})s, && (22) \\ y(s) &= -\frac{2}{m^2}\mathrm{dn}(s|k), && (23) \end{aligned}$$

where $E(s|m)$ is the incomplete elliptic integral of the second kind with modulus m. Again, if we take $L = 2K(m)$, then since $\theta(s = \pm K(m)) = \pm\pi$, these solutions correspond to clamped boundary conditions but result in self-intersecting shapes. The equilibrium shapes corresponding to (14) and (19) are plotted in Figure 1 for various values of m.

Periodic boundary conditions

In the special case of $k = 0$ (which implies $b = 0$) it is possible to recast (10) as

$$\frac{d}{ds}\left(\left(\frac{1}{2}\frac{d\kappa}{ds}\right)^2 + \frac{\kappa^4}{8} + \frac{C\kappa^2}{2}\right) = 0, \tag{24}$$

which implies

$$\left(\frac{1}{2}\frac{d\kappa}{ds}\right)^2 + \frac{\kappa^4}{8} + \frac{C\kappa^2}{2} = B, \tag{25}$$

where B is a constant. This results in closed orbits on the $\kappa - \frac{d\kappa}{ds}$ plane which suggests periodic solutions for $\kappa(s)$. One class of periodic solution in terms of elliptic functions is given by

$$\kappa(s) = 2m\mathrm{cn}(s|m), \tag{26}$$

which results in

$$\begin{aligned} x(s) &= 2E(s|m) - s, \\ y(s) &= 2m\mathrm{cn}(s|m), \\ \theta(s) &= 2\cos^{-1}(\mathrm{dn}(s|m)), \end{aligned} \tag{27}$$

where $E(s|m)$ is the incomplete elliptic integral of the second kind with modulus m [17]. Figure 2 (I) shows the equilibrium shapes for various values of m.

Another class of shapes that solve (10) with $b = 0$ is given by

$$\kappa(s) = 2m\sqrt{1-m^2}\frac{\mathrm{sn}(s|m)}{\mathrm{dn}(s|m)}. \tag{28}$$

To realize periodic boundary conditions, we set $L = 4qK(m)$ where $K(m)$ is the complete elliptic integral of the first kind and q is a positive integer. By integration we get

$$\theta(s) = 2\sin^{-1}\left(-m\frac{\mathrm{cn}(s|m)}{\mathrm{dn}(m|k)}\right), \tag{29}$$

$$\cos(\theta) = 1 - 2m^2\frac{\mathrm{cn}^2(s|m)}{\mathrm{dn}^2(s|m)}, \tag{30}$$

$$\sin(\theta) = -2m\sqrt{1-k^2}\frac{\mathrm{cn}(s|m)}{\mathrm{dn}^2(s|m)}. \tag{31}$$

We obtain $x(s)$ and $y(s)$ by integrating numerically. The equilibrium shapes thus obtained are plotted in Figure 2 (II) for various values of m and $q = 1$.

Simply supported boundary conditions

Interestingly, (26) and (27) will also be a solution to (10) with $k = \rho g$ if we select the arbitrary constant C as

$$\frac{C}{K_b} = 1 - 2m^2 - \frac{\rho g}{K_b}. \tag{32}$$

Here, as before, m must be determined from the boundary conditions. The appropriate boundary condition is

$$x\left(\frac{L}{2}\right) - x\left(-\frac{L}{2}\right) = 4E\left(\frac{L}{2}\middle| m\right) - L = \frac{L}{1+\epsilon_{pre}}, \tag{33}$$

where ϵ_{pre} is a pre-strain or is determined from the compression applied on the film. For given L this is an equation for m which can be solved numerically. We also see that $y(s = K(m)) = 0$ and $\theta(s = K(m)) \neq 0$ where $K(m)$ is the complete elliptic integral of the first kind. This means that (26) and (27) are solutions of (10) with simply supported boundary conditions with $L = 2K(m)$ which correspond to zero deflection and zero curvature at the two ends. Note that $\theta(s)$ in (27) can be written as

$$\theta(s) = 4\tan^{-1}\left(\frac{m\mathrm{sn}(s|m)}{1+\mathrm{dn}(s|m)}\right). \tag{34}$$

This is reminiscent of the solution in [3] where the symmetric solution for clamped-clamped boundary conditions was

$$\theta(s) = 4\tan^{-1}\left(\frac{\kappa\sin(ks)}{k\cosh(\kappa s)}\right), \tag{35}$$

with $k^2 + \kappa^2 = 1$. Although these solutions correspond to different boundary conditions, they look similar if we take $\kappa << 1$ and $m^2 = 2\kappa + \kappa^3$ (which would mean a small ϵ_{pre}).

ASYMMETRIC SHAPES

All of the analytical solutions derived in the previous section give rise to symmetric equilibrium shapes. In experiments, however, many asymmetric shapes are commonly observed (e.g., in [2]). In this section, we develop a numerical procedure to obtain such shapes. First, we recast our problem as a system of first order ODEs (using equations (5) through (9)):

$$\begin{aligned}
\frac{dx}{ds} &= \cos\theta, && (36)\\
\frac{dy}{ds} &= \sin\theta, && (37)\\
\frac{d\theta}{ds} &= \frac{M}{K_b}, && (38)\\
\frac{dM}{ds} &= -F_n, && (39)\\
\frac{dF_n}{ds} &= ky + \frac{K_b}{2}\frac{M^3}{K_b^3} + C\frac{M}{K_b}. && (40)
\end{aligned}$$

In the experiments of [2] the end-to-end distance $x(L/2) - x(-L/2)$ is reduced in order to buckle the film. We account for this by using a strain ϵ_{pre} through our boundary conditions:

$$\begin{aligned}
x(L/2) - x(-L/2) &= \frac{L}{1+\epsilon_{pre}}, && (41)\\
y(-L/2) = 0, \quad y(L/2) &= 0, && (42)\\
\theta(-L/2) = 0, \quad \theta(L/2) &= 0. && (43)
\end{aligned}$$

We solve the system consisting of (36) through (43) numerically. Details of the solver are presented in the appendix. Select solutions are plotted in Figures 3 to 4 with the following motivation. First, in Figure 3, we show solutions that closely match the experimentally obtained shapes reported in Figure 1(A) of [2]. Second, odd and even type solutions for varying ϵ_{pre} values along with the corresponding internal moment M and normal force F_n are shown in Figures 8 and 9 respectively that correspond to the antisymmetric and symmetric configurations derived analytically in [3]. Lastly, we plot a few classes of general multiple fold shapes in Figure 4. The advantage of our approach is that all of these shapes can also be obtained by using the same solver.

FLUID-STRUCTURE INTERACTION PROBLEM

Consider a planar elastic membrane suspended in an incompressible viscous fluid with viscosity μ. The fluid domain Ω is assumed to be periodic in the $x-$direction and unbounded in the $y-$direction. Let $\mathbf{x}$ be the position of the membrane γ, $\mathbf{v}$ the fluid velocity, and p the pressure. In the vanishing Reynolds number limit, the governing equations for the ambient fluid are given by

$$\begin{aligned}
-\mu\Delta\mathbf{v} + \nabla p = \mathbf{0} \text{ in } \Omega\backslash\gamma,\\
\nabla\cdot\mathbf{v} = 0 \text{ in } \Omega\backslash\gamma.
\end{aligned} \tag{44}$$

The fluid motion is coupled to the membrane motion via the kinematic boundary condition

$$\dot{\mathbf{x}} = \mathbf{v} \quad \text{on} \quad \gamma. \tag{45}$$

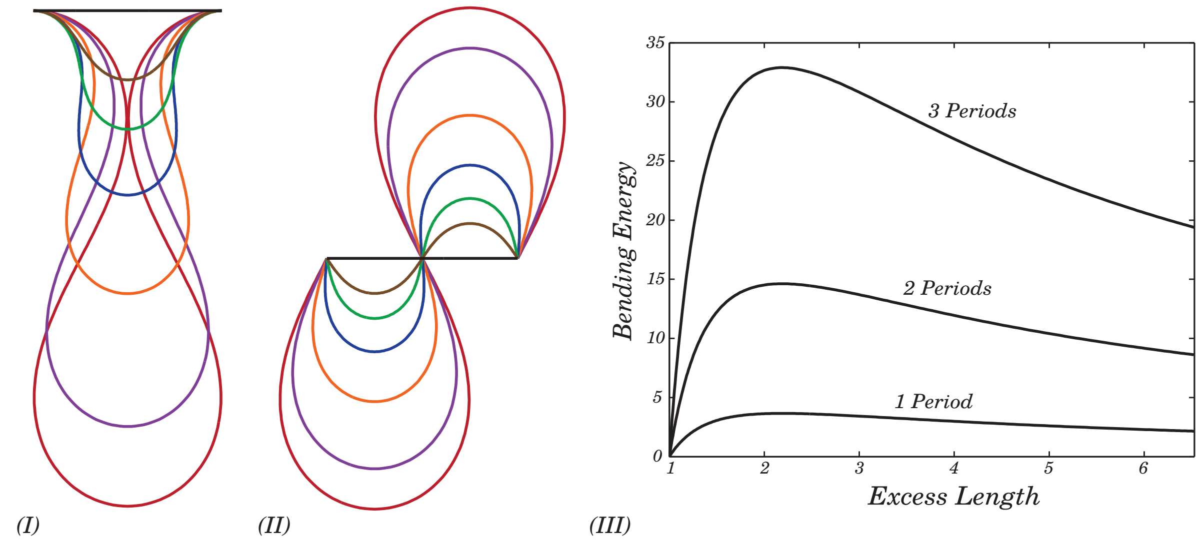

FIG. 2: *(Color online) Plots of equilibrium shapes corresponding to the exact solutions (26) and (28) in (I) and (II) respectively for various excess lengths (with shapes colored the same in (I) and (II) representing those with same value for m). Excess length is defined as the membrane arc length over the period 2π. Periodicity implies that multiple fold shapes obtained by concatenating each of these exact solutions is also an exact solution but with a higher excess length. In (III), we compare the bending energy, defined as $\int_{\gamma(s)} \kappa^2(s)\, ds$, of the shapes in (I) plotted over multiple periods and proportionally scaled back to $[0, 2\pi)$ (for example, a four-fold and a two-fold shapes are plotted in Figure 7).*

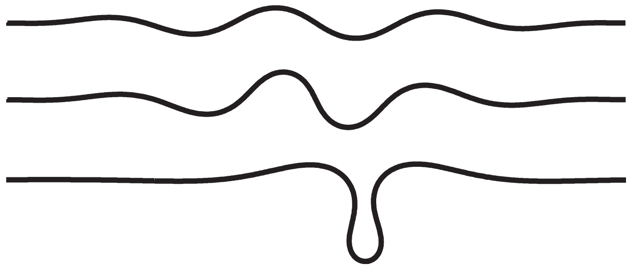

FIG. 3: *Equilibrium shapes obtained by solving (36) through (43) that match the experimentally observed shapes reported in Fig. 1(A) of [2]. The solutions were obtained by modifying ϵ_{pre} while varying L to hold $x(L/2)$ constant. The first and second solutions from the top are odd type solutions as shown in Fig. 8. The last solution is an even type solution like those shown in Fig. 9.*

The local inextensibility constraint on the membrane can be expressed as [18]

$$\mathbf{x}_s \cdot \dot{\mathbf{x}}_s = 0 \text{ on } \gamma. \tag{46}$$

The stress balance at the membrane interface is given by

$$[\![-p\mathbf{n} + (\nabla \mathbf{v} + \nabla \mathbf{v}^T)\mathbf{n}]\!] = \mathbf{f}_{mem} \text{ on } \gamma, \tag{47}$$

where $\mathbf{n}$ is the unit normal to the membrane. The notation $[\![q]\!]$ denotes the jump of a quantity q across the membrane. The classical Helfrich energy model for the bilayer membrane and an augmented Lagrangian approach (to enforce the local inextensibility) lead to a bending force $\mathbf{f}_b$ and a tension force $\mathbf{f}_\sigma$ on the membrane so that $\mathbf{f}_{mem} = \mathbf{f}_b + \mathbf{f}_\sigma$. They are defined by [18]

$$\mathbf{f}_b = -\kappa_B \mathbf{x}_{ssss}, \quad \mathbf{f}_\sigma = (\sigma \mathbf{x}_s)_s, \tag{48}$$

where κ_B is the bending modulus, κ is the curvature, s is the arclength parameter, and σ is the tension which acts as a Lagrange multiplier to enforce the local inextensibility constraint.

Given an arbitrary initial shape, the membrane deforms until the elastic stress due to bending and tension balances out the hydrodynamic stress at the interface. The transient dynamics can be simulated by solving the the fluid equations subject to the no-slip, periodic, and kinematic boundary conditions along with the stress balance. We use potential theory to recast the governing equations for the membrane evolution in the form of coupled integro-differential equations:

$$\begin{aligned} \dot{\mathbf{x}} = \int_\gamma G(\mathbf{x}, \mathbf{y})\, (\mathbf{f}_b(\mathbf{y}) + \mathbf{f}_\sigma(\mathbf{y}))\; \mathrm{d}\gamma(\mathbf{y}), \\ \mathbf{x}_s \cdot \dot{\mathbf{x}}_s = 0, \end{aligned} \tag{49}$$

where G is the periodic Green's function for the Stokes equations (44), which is known in closed analytic form[1].

---

[1] It is given by [19]:

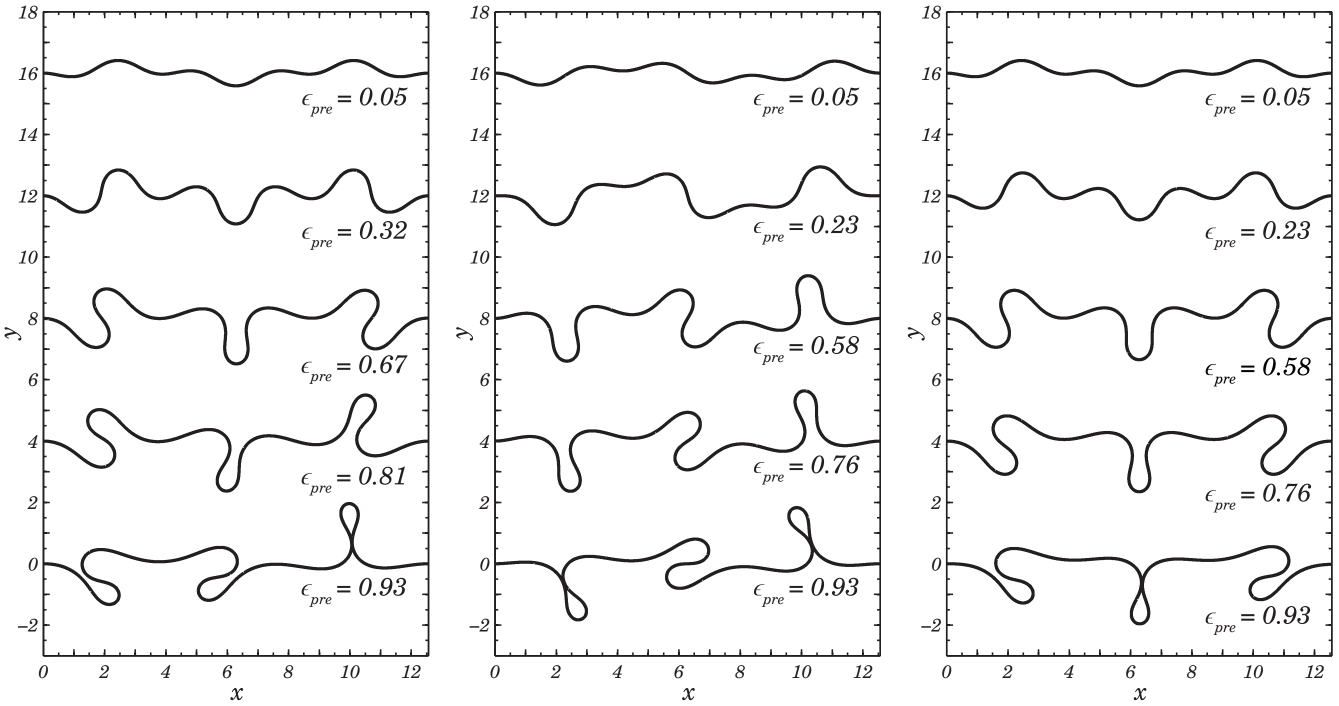

FIG. 4: *Other classes of equilibrium shapes that can be obtained by solving* (36) *through* (43)*. The solutions were obtained by numerically continuing* ϵ_{pre} *from the folded solution to the low amplitude solution while varying* L *to keep* $x(L/2)$ *constant.*

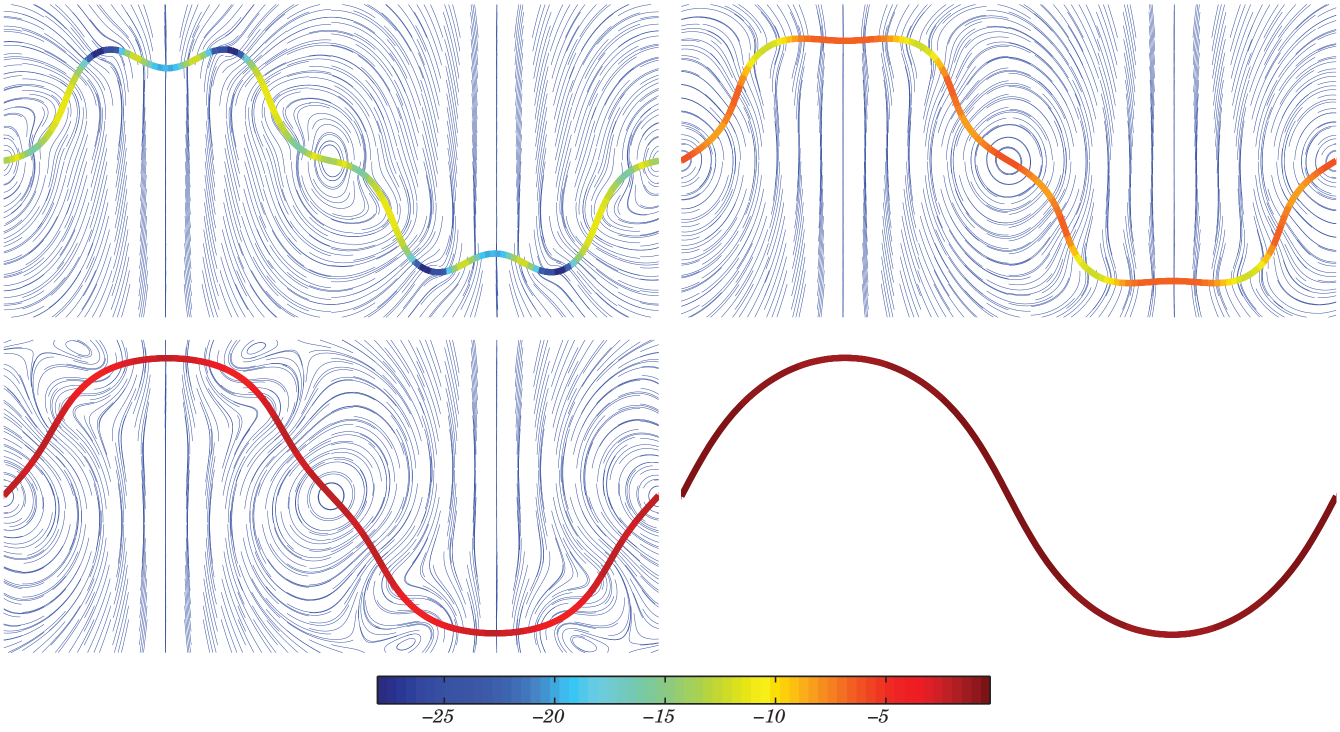

FIG. 5: *(Color online) Snapshots of a bilipid membrane evolving to an equilibrium shape starting from an arbitrary initial shape. The streamlines are determined by evaluating the surrounding fluid velocity using the relation* $\mathbf{v}(\mathbf{x}) = \int_\gamma G(\mathbf{x}, \mathbf{y})\, \mathbf{f}_{mem}$ *for any* $\mathbf{x}$ *in the fluid domain. The color on the membrane indicates the magnitude of the tension* σ*.*

The integral equation formulation (49) has two important advantages. First, the Green's function satisfies the fluid incompressibility condition and the far-field (periodic) boundary condition by construction. Second, the unknowns reside only on the membrane. This avoids the need for a volume mesh. We describe our numerical scheme to solve (49) next.

NUMERICAL SCHEME

We represent the membrane orientation as a parametrized curve. Each value of $\alpha \in [0, 2\pi)$ is a reference to a point $\mathbf{x}(\alpha, t) = [x(\alpha, t),\, y(\alpha, t)]^T$ on the membrane. Denoting by L the total arc length of the membrane, the x-component of the membrane position can be expressed as the sum of a linear term and a function x_p that is 2π-periodic in α:

$$x(\alpha, t) = \frac{L}{2\pi}\alpha + x_p(\alpha, t). \tag{50}$$

We track the evolution of marker points on the membrane that are uniformly spaced in the parametric domain at $\{\alpha_j = 2\pi(j-1)/M\}_{j=1}^{M}$ for a given discretization size M. This allows fast and spectrally accurate computation of derivatives via the fast Fourier transform (FFT). For example, we can write

$$y_\alpha = \sum_{j=-M/2}^{M/2} (-ij)\hat{y}(j)e^{-ij\alpha}, \tag{51}$$

and use FFTs to switch between y and $\hat{y}$.

The periodic Stokes Green's function in (49), similar to its free-space counterpart, exhibits a logarithmic singularity to the leading order when the evaluation point $\mathbf{x}$ resides on the membrane [19]. Therefore, quadrature rules designed for smooth integrands such as the trapezoidal rule are not effective in evaluating the integral in (49), and a special treatment is required. We use the hybrid Gauss-trapezoidal quadrature rule outlined in [20] that is designed to yield arbitrarily high-order accuracy for integrals of this form. We evaluate the integrand at the small number of nonuniform Gaussian nodes this rule requires via Fourier interpolation.

Time-stepping scheme

We propose the following time-stepping scheme for the membrane orientation and inextensiblity equations (49):

$$\frac{\mathbf{x}^{k+1} - \mathbf{x}^{k}}{\Delta t} = \int_{\gamma^k} G(\mathbf{x}^k, \mathbf{y}^k)[(\sigma^{k+1}\mathbf{y}^k{}_s)_s - \kappa_B \mathbf{y}^{k+1}_{ssss}]\,\mathrm{d}\gamma, \tag{52}$$

$$0 = \mathbf{x}^k_s \cdot \left(\int_{\gamma^k} G(\mathbf{x}^k, \mathbf{y}^k)[(\sigma^{k+1}\mathbf{y}^k{}_s)_s - \kappa_B \mathbf{y}^{k+1}_{ssss}]\,\mathrm{d}\gamma\right)_s. \tag{53}$$

All derivatives are computed using the membrane orientation from the kth time step. This semi-implicit discretization is based on [18] and has been shown to have unconditional stability. If we let $\mathbf{v} = [x,\, y,\, \sigma]^T$, then it may be verified that the following are linear operators:

$$\mathcal{B}(\mathbf{v}) = \mathbf{x} - \Delta t \int_{\gamma^k} G(\mathbf{x}^k, \mathbf{y}^k)[(\sigma\mathbf{y}^k{}_s)_s - \kappa_B \mathbf{y}_{ssss}]\,\mathrm{d}\gamma, \tag{54}$$

$$\mathcal{D}(\mathbf{v}) = \mathbf{x}^k_s \cdot \left(\int_{\gamma^k} G(\mathbf{x}^k, \mathbf{y}^k)[(\sigma\mathbf{y}^k{}_s)_s - \kappa_B \mathbf{y}_{ssss}]\,\mathrm{d}\gamma\right)_s, \tag{55}$$

where $\mathbf{x} = \mathbf{y} = [x,\, y]^T$. This yields the linear system

$$\mathcal{B}(\mathbf{v}) = \mathbf{x}^k, \qquad \mathcal{D}(\mathbf{v}) = 0, \tag{56}$$

whose solution gives the functions $\mathbf{x}^{k+1}(\alpha)$ and $\sigma^{k+1}(\alpha)$ at the next time step. This linear system, as it is stated now, is not ideal for a number of reasons. First, x should maintain the form $x(\alpha) = L\alpha/2\pi + x_p(\alpha)$ throughout the entire computation. Any nonunitary scaling of x that happens within the linear solver would change the linear term and as a result, invalidate our assumption about the form of x. Another issue is that when x is rescaled by the linear solver, the logarithmic singularities in the integral operators $\mathcal{B}$ and $\mathcal{D}$ will move so that applying the quadrature will be nontrivial. We handle this by decomposing $\mathbf{v}$ as follows:

$$\mathbf{v} = \begin{bmatrix} x \\ y \\ \sigma \end{bmatrix} = \begin{bmatrix} L\alpha/2\pi \\ 0 \\ 0 \end{bmatrix} + \begin{bmatrix} x_p \\ y \\ \sigma \end{bmatrix} = \begin{bmatrix} L\alpha/2\pi \\ 0 \\ 0 \end{bmatrix} + \mathbf{v}_p. \tag{57}$$

This gives us the system

$$\mathcal{B}(\mathbf{v}_p) = \mathbf{x}^k - \mathcal{B}_L, \qquad \mathcal{D}(\mathbf{v}_p) = -\mathcal{D}_L, \tag{58}$$

where

$$\mathcal{B}_L = \mathcal{B}([L\alpha/2\pi,\, 0,\, 0]^T), \qquad \mathcal{D}_L = \mathcal{D}([L\alpha/2\pi,\, 0,\, 0]^T). \tag{59}$$

With this change, all input functions x_p, y, and σ are periodic so that scaling $\mathbf{v}_p$ will no longer jeopardize the form of x. We use the GMRES method [21] to solve this linear system.

Note that, since $[L\alpha/2\pi, 0, 0]_s^T$ is periodic, computing $\mathcal{B}_L$ and $\mathcal{D}_L$ leads to a periodic integrand, as is the case with $\mathbf{v}_p$. Since the integrand is periodic, we may shift it so that the logarithmic singularity is always at the two ends of the interval $[0, 2\pi)$. We then apply the quadrature rule of [20] on the intervals $[0,\ \pi)$ and $[\pi,\ 2\pi)$ separately.

COMPUTATIONAL RESULTS

In this section, we perform an error analysis on the numerical scheme. We begin the program with an arbitrary initial profile and allow it to evolve in time in order to verify that the inextensibility of the membrane and the incompressibility of the fluid are preserved. We check that as the number of spatial grid points is increased and the size of the time-step is decreased, the relative error approaches zero. Later, the program is tested on one of the analytic equilibrium shapes with periodic boundary conditions. We do this by computing the initial membrane velocity on the shape. If it is indeed an equilibrium solution, then the velocity should approach zero as the resolution of the numerical scheme is enhanced.

Error analysis

We test that the program preserves membrane inextensibility and fluid incompressibility by evolving the curve

$$x(\alpha) = \alpha, \quad y(\alpha) = \exp(\sin\alpha + 0.1\cos 5\alpha), \qquad (60)$$

until $t = 0.32$. We let $\Delta t = 0.004/M$ where M is the number of spacial grid points. The evolution of the curve and its bending energy are shown in Figure 6. If membrane inextensibility is preserved, we expect the relative error between the initial membrane arc length L_0 and the final membrane arc length L_f to approach zero as M increases. Similarly, fluid incompresibility should imply that the area under the membrane remains constant. The area considered is the region contained by the x-axis and the membrane. The results of our error analysis are shown in Table I. We observe a first order asymptotic convergence for the length and area. This is in accordance with our first order time-stepping scheme.

Equilibrium shapes

We numerically verify that one of the analytic shapes derived above is an equilibrium solution. This will be done using two approaches. First, we check that the single-layer potential approaches zero as M, the number of spatial grid points, increases. This would indicate an initial velocity of zero. Second, we run the program until $t = 1$ using $\Delta t = 0.32/M$. As M increases, the difference between the initial and final membrane orientations should approach zero. Table II summarizes the results for the shape with one period and excess length equal to 5.09. For both approaches we obtain rapid convergence to zero. This is as expected, since the singular integrals were computed using the eigth-order Gauss-Trapezoidal scheme, and all derivatives have spectral convergence.

TABLE I: *Convergence analysis of our numerical scheme measured on the basis of preserving the membrane inextensibility and fluid incompressibility constraints. Here, M is the number of spatial discretization points and the time-step size Δt is reduced by half as M is doubled. We report the relative errors in the length of the membrane L and area under it A measured at the end of the simulation in figure 6. We observe a first-order asymptotic convergence for the length and the area, which is consistent with our time-stepping scheme.*

M	64	128	256
$\lvert L_0 - L_f\rvert/L_0$	$3.314 \cdot 10^{-4}$	$1.790 \cdot 10^{-4}$	$9.368 \cdot 10^{-5}$
$\lvert A_0 - A_f\rvert/A_0$	$3.939 \cdot 10^{-6}$	$1.746 \cdot 10^{-6}$	$9.111 \cdot 10^{-7}$

TABLE II: *The analytical solutions in figure 2 (I) are verified by feeding them as initial shapes to our membrane-fluid solver and checking that the resultant velocity field is zero. We report the maximum magnitude values for the initial velocity field evaluated on the membrane in the second row. We simulate the evolution to a fixed time horizon and report the max-norm error in the difference of initial and final positions in the third row. Clearly, both the errors converge to zero verifying that these are indeed the equilibrium shapes.*

M	32	64
$\lVert\mathbf{v}(\mathbf{x})\rVert_\infty$	$3.043 \cdot 10^{-7}$	$2.797 \cdot 10^{-10}$
$\lVert\mathbf{x}_0 - \mathbf{x}_f\rVert_\infty$	$6.978 \cdot 10^{-9}$	$6.630 \cdot 10^{-11}$

Finally, a natural question that arises is whether the multiple-fold shapes as discussed in Figure 2 are in fact stable equilibria. To verify this, we can take one of our analytical equilibrium shapes with multiple folds as the initial condition to the fluid-structure interaction problem and check if the shape changes over time. The result of one such numerical experiment is plotted in Figure 7. As is evident, the shape tends to remain the same until the numerical errors perturb it from this local equilibrium to a shape with lower number of folds. The timescales for these transitions from higher-to-lower energy states are found to be entirely dependent on the numerical parameters such as the discretization and time-step sizes.

CONCLUSIONS

We provided a rod theory based approach for determining the equilibrium profiles that arise when a thin elastic membrane is subjected to either clamped, simply supported or periodic boundary conditions. In the former case, we showed that a larger family of quasi-static equilibrium shapes exist. We derived a system of ODEs

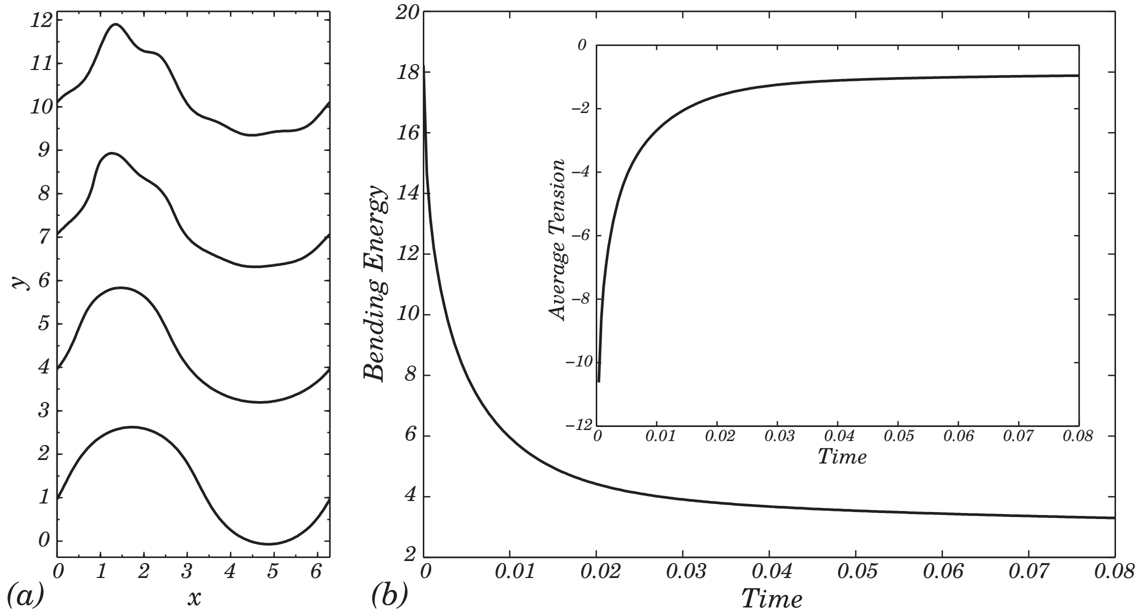

FIG. 6: *(a) Membrane shapes in time as it relaxes to equilibrium in a quiescent flow. (b) Plots of the membrane bending energy and average tension as a function of time.*

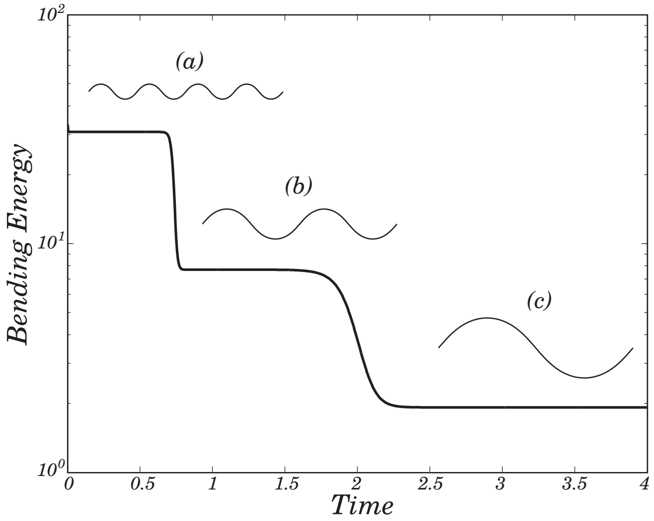

FIG. 7: *Evolution of a membrane with (a) four-fold shape to (b) two-fold shape to (c) a single-fold shape, in quiescent flow (see supplementary material for an animation). While the multiple-fold shapes have higher bending energy (as also pointed out in Figure 2), they correspond to stable equilibria.*

that when solved by the provided numerical routine, produced these more general multiple-fold solutions, along with the previously known shapes. The implementation of this routine is quick, and solutions can be generated in a matter of seconds.

In the case of periodic boundary conditions, we provided analytical solutions in terms of elliptic functions and solved the fluid-structure interaction problem using a boundary integral formulation. Our numerical scheme is unconditionally stable and converges spatially with spectral accuracy. We were able to verify our analytical solutions by showing that their initial velocity quickly converged to zero as the resolution of the solver was increased. In addition, we found that for any arbitrary initial profile, the membrane always relaxed back to one of the analytically obtained equilibrium shapes.

ACKNOWLEDGMENTS

We acknowledge helpful discussions with Yuan Young. GRM and SV acknowledge support from NSF under Grants DMS-1224656 and DMS-1418964. PKP acknowledges partial support from the Army Research Office through grant number W911NF-11-1-0494. This research was supported in part through computational resources and services provided by Advanced Research Computing at the University of Michigan, Ann Arbor.

APPENDIX

Numerical solution of rod theory equations

The system consisting of (36) through (43) is numerically solved using a shooting method based routine. A shooting method works by reducing the solution of a boundary value problem to the solution of an initial value problem. This is done by determining a set of initial conditions that yields a solution that satisfies the desired boundary conditions. Since the first boundary condition relies on the difference between $x(L/2)$ and $x(-L/2)$, we may let $x(-L/2) = 0$ and then require

$$x(L/2) = \frac{L}{1+\epsilon_{pre}}. \tag{61}$$

Next, we let

$$C = \lambda_1, \quad M(-L/2) = \lambda_2, \quad F_n(-L/2) = \lambda_3. \tag{62}$$

For a given triplet of λ-values $(\lambda_1, \lambda_2, \lambda_3)$ we have the initial conditions

$$\begin{aligned} x(-L/2) &= 0, \\ y(-L/2) &= 0, \\ \theta(-L/2) &= 0, \\ M(-L/2) &= \lambda_2, \\ F_n(-L/2) &= \lambda_3. \end{aligned} \tag{63}$$

We may now step forward in time using a time-stepping routine, such as Matlab's `ode45` which uses a variable step Runge-Kutta method. At $s = L/2$ we obtain

$$x_{L/2}(\lambda_1, \lambda_2, \lambda_3) = x(L/2), \tag{64}$$

$$y_{L/2}(\lambda_1, \lambda_2, \lambda_3) = y(L/2), \tag{65}$$

$$\theta_{L/2}(\lambda_1, \lambda_2, \lambda_3) = \theta(L/2). \tag{66}$$

If a given triplet of λ-values yields a solution that satisfies (42), (43), and (61), then

$$\mathcal{E}(\lambda_1, \lambda_2, \lambda_3) = \left[\, x_{L/2} - \tfrac{L}{1+\epsilon_{pre}},\ y_{L/2},\ \theta_{L/2} \,\right]^T \tag{67}$$

will equal the zero vector. That is, $\mathcal{E}$ is a mapping from $\mathbb{R}^3$ to $\mathbb{R}^3$ whose roots correspond to solutions of the BVP. These roots can be found using Newton's method. We use Matlab's `fsolve` routine to solve for them.

---

[1] B. Li, Y.-P. Cao, X.-Q. Feng, and H. Gao, Soft Matter **8**, 5728 (2012).

[2] L. Pocivavsek, R. Dellsy, A. Kern, S. Johnson, B. Lin, K. Y. C. Lee, and E. Cerda, Science (2008).

[3] H. Diamant and T. A. Witten, Physical review letters **107**, 164302 (2011).

[4] O. Oshri, F. Brau, and H. Diamant, arXiv preprint arXiv:1503.01674 (2015).

[5] M. Rivetti, Comptes Rendus Mécanique **341**, 333 (2013).

[6] M. Rivetti and S. Neukirch, Journal of the Mechanics and Physics of Solids **69**, 143 (2014).

[7] R. Lipowsky, Nature **349**, 475 (1991).

[8] Z. Shao-guang and O. Zhong-can, Phys. Rev. E **53**, 4206 (1996).

[9] Y. Deng, M. Marko, K. F. Buttle, A. Leith, M. Mieczkowski, and C. A. Mannella, J. Struc. Biol. **127**, 231 (1999).

[10] Z. Almsherqi, S. Hyde, M. Ramachandran, and Y. Deng, J. R. Soc. Interface **5**, 1023 (2008).

[11] R. Zeineldin, J. A. Last, A. L. Slade, L. K. Ista, P. Bisong, M. J. O'Brien, S. R. J. Brueck, D. J. Sasaki, and G. P. Lopez, Langmuir **22**, 8163 (2006).

[12] J. Fan, T. Han, and M. Haataja, The Journal of chemical physics **133**, 235101 (2010).

[13] Y.-N. Young, S. Veerapaneni, and M. J. Miksis, Journal of Fluid Mechanics **751**, 406 (2014), ISSN 1469-7645.

[14] S. K. Veerapaneni, R. Raj, G. Biros, and P. K. Purohit, International Journal of Non-Linear Mechanics **44**, 257 (2009).

[15] J. E. Rim, P. K. Purohit, and W. S. Klug, Biomechanics and modeling in mechanobiology pp. 1–12 (2014).

[16] S. S. Antman, *Nonlinear problems of elasticity*, vol. 107 (Springer, 2005).

[17] N. J. Agrawal, R. Radhakrishnan, and P. K. Purohit, Biophysical journal **94**, 3150 (2008).

[18] S. K. Veerapaneni, D. Gueyffier, D. Zorin, and G. Biros, Journal of Computational Physics **228**, 2334 (2009).

[19] C. Pozrikidis, *Boundary Integral and Singularity Methods for Linearized Viscous Flow* (Cambridge University Press, Cambridge, 1992).

[20] B. K. Alpert, SIAM Journal on Scientific Computing **20**, 1551 (1999).

[21] Y. Saad, *Iterative methods for sparse linear systems* (Siam, 2003).

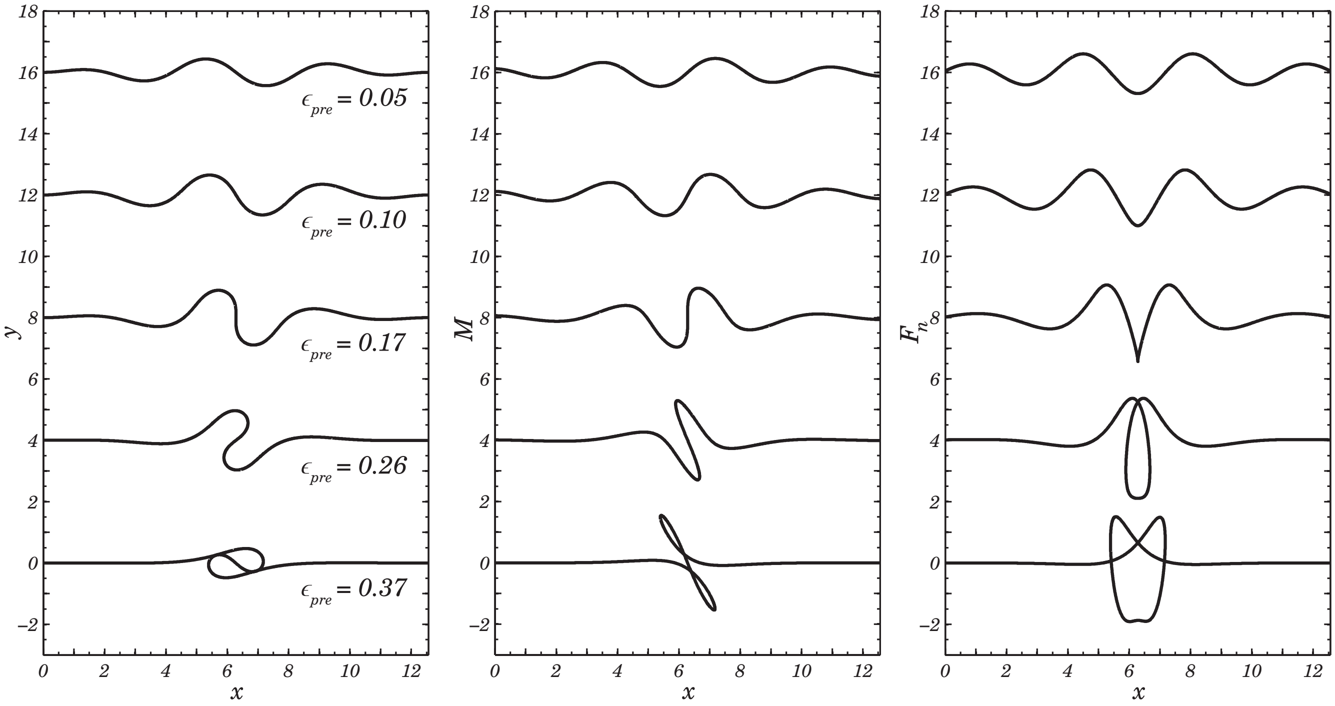

FIG. 8: *Odd type equilibrium shapes for different values of ϵ_{pre} along with the internal moments M and the normal component of the internal force F_n obtained by solving* (67)*. Plots were shifted vertically by 4 for spacing.*

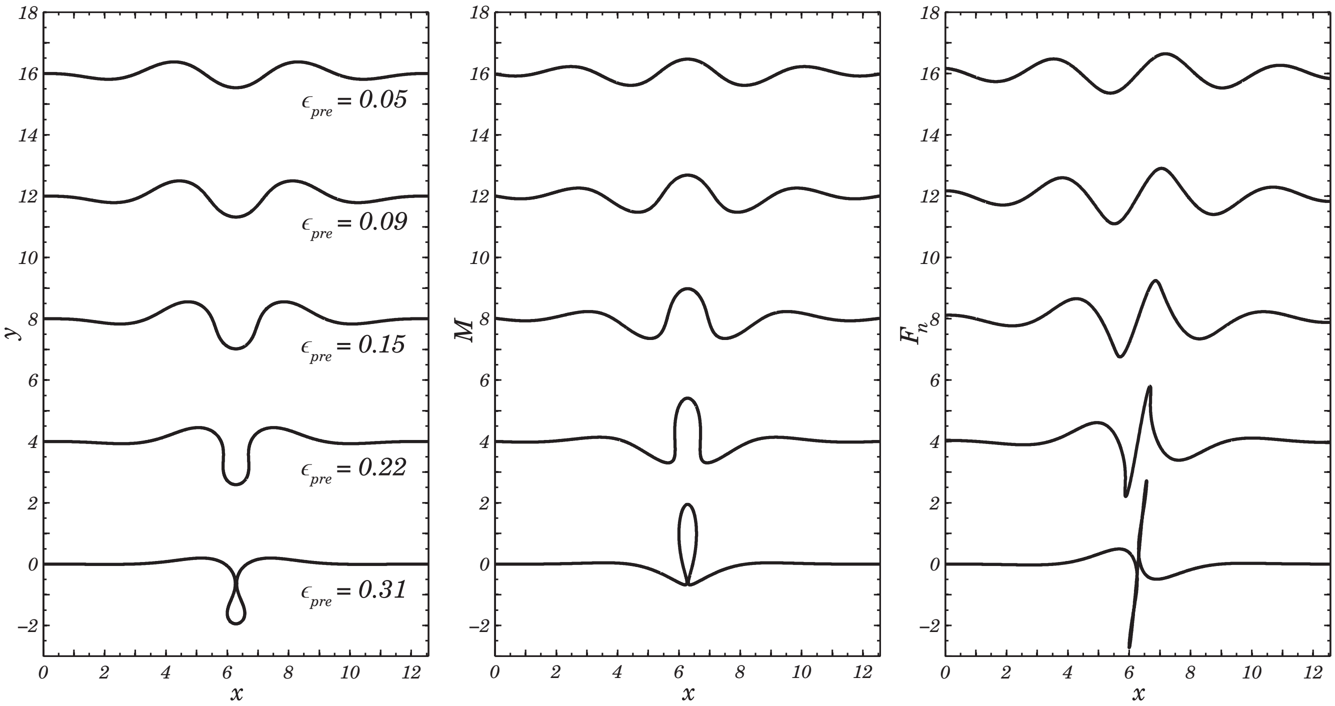

FIG. 9: *Even type equilibrium shapes for different values of ϵ_{pre} along with the internal moments M and the normal component of the internal force F_n obtained by solving* (67)*. Plots were shifted vertically by 4 for spacing.*